ANTHROPOLOGY

Human dispersals out of Africa via the Levant

Mahmoud Abbas[1], Zhongping Lai[1]*, John D. Jansen[2], Hua Tu[1]*, Mohammad Alqudah[3], Xiaolin Xu[1], Bety S. Al-Saqarat[4], Mu'ayyad Al Hseinat[4], Xianjiao Ou[5], Michael D. Petraglia[6,7,8], Paul A. Carling[9,10,11]

Homo sapiens dispersed from Africa into Eurasia multiple times in the Middle and Late Pleistocene. The route, across northeastern Africa into the Levant, is a viable terrestrial corridor, as the present harsh southern Levant would probably have been savannahs and grasslands during the last interglaciation. Here, we document wetland sediments with luminescence ages falling in the last interglaciation in the southern Levant, showing protracted phases of moisture availability. Wetland sediments in Wadi Gharandal containing Levallois artifacts yielded an age of 84 ka. Our findings support the growing consensus for a well-watered Jordan Rift Valley that funneled migrants into western Asia and northern Arabia.

INTRODUCTION

Our species, *Homo sapiens*, evolved in Africa between ~300 and 200 thousand years (ka) ago (*1–3*) and dispersed out of the continent during multiple episodes, including Marine Isotope Stage (MIS) 5 (129 to 71 ka) (*4–6*). The geographical routes of dispersal into Eurasia have been long debated, e.g., the northern route from the Sinai Peninsula to the southern Levant then to Arabia, and the southern route via the Bab El Mandeb strait into the margins of southern Arabia (Fig. 1A) (*7–10*). The southern route, i.e., the Red Sea crossing, is regarded as possible in glacial periods with low sea level (*7, 8, 11*). On the other hand, the dispersal via the northern corridor during ~130 to 90 ka has been considered the most viable route in MIS 5 (*12, 13*), given a growing number of archaeological and paleontological discoveries. These discoveries include hominin fossils and artifacts from the well-known caves of the Mediterranean Levant (Fig. 1B) (*5, 6, 14, 15*) and the fossil finds, human footprints, and Middle Paleolithic artifacts from the Nefud Desert dated to between ~120 and 85 ka (*4, 16*).

Recent studies suggest that dispersal routes were associated with well-watered corridors that facilitated hominins to move into Eurasia (*4, 17–20*). Investigations in northern, central, and southern parts of Arabia showed that these areas were habitable in MIS 5, in particular for substages MIS 5e (128 to 121 ka), 5c (104 to 97 ka), 5a (82 to 77 ka), and in MIS 3 (~54 ka), owing to climatic amelioration and enhanced humidity [e.g., (*4, 10, 16, 21–25*)]. However, climatic and paleoenvironmental archives from the southern Levant and Jordan, as a vital migration corridor, are not well understood owing to the poor chronological framework of the paleo-water bodies in the region (*26–29*).

Widely distributed paleo-aquatic sediments in the Jordan Rift Valley and on the Jordanian Plateau previously were dated to MIS 3 and the Last Glacial Maximum by radiocarbon dating of charcoal and organic matters in sediments (*27, 30, 31*). More extensive field investigation and results of optically stimulated luminescence (OSL) dating recently suggest that these sediments were formed ca. 120 to 65 ka (*18, 32*). The present study provides a systematic luminescence chronology using quartz OSL and feldspar post–infrared-infrared–stimulated luminescence (pIR-IRSL) for three paleo-water bodies in the Jordan desert: Wadi Hasa, west-central Jordan, Gregra, and Wadi Gharandal along the Jordan River Valley. The current chronology has a bearing on key discussions related to the regional climate and hominin and mammalian biogeography, due to the critical geographic position of the three studied wetlands along the northern route proximate to Africa.

RESULTS

Wadi Gharandal

All the luminescence dating results are listed in Table 1 and shown in Fig. 2. In Wadi Gharandal the paludal sediments were formed during ca. 125 to 70 ka (GH2 and GH3 in Fig. 2 and fig. S1A). Three in situ lithic tools were found at a depth of 1.25 m at GH3, and two were identified as Levallois flakes (the inset in Fig. 2). Two luminescence samples were obtained from section GH3 (Fig. 2). Sample GH3-OSL2 at a depth of 1.05 m had a quartz OSL age of 71 ± 5 ka and a single-grain feldspar pIR-IRSL$_{290}$ age of 65 ± 10 ka, and GH3-OSL3, at a depth of 1.25 m from the same sediment layer containing the Levallois flakes, yielded ages of 84 ± 5 ka by quartz OSL and 72 ± 6 ka by feldspar single-grain pIR-IRSL$_{290}$ method. The measured quartz OSL D_e of sample GH3-OSL3 is 161 ± 5 grays (Gy), while the $2D_0$ yielded a value of 154 Gy, indicating a potential saturation. However, the quartz OSL age (84 ± 5 ka) and feldspar single-grain pIR-IRSL$_{290}$ age (72 ± 6 ka) of this sample (84 ± 5 ka and 72 ± 6 ka) are close to each other considering the age uncertainty. The single-grain feldspar pIR-IRSL$_{290}$ age (65 ± 10 ka) for sample GH3-OSL2 also shows consistency with quartz OSL age (71 ± 5 ka), considering the age uncertainty.

[1]Institute of Marine Sciences, Guangdong Provincial Key Laboratory of Marine Disaster Prediction and Prevention, Shantou University, Shantou 515063, China. [2]GFU Institute of Geophysics, Czech Academy of Sciences, Prague, Czechia. [3]Department of Earth and Environmental Sciences, Faculty of Science, Yarmouk University, 211163 Irbid, Jordan. [4]School of Science, Geology Department, University of Jordan, Amman, Jordan. [5]School of Geography and Tourism, Jiaying University, Meizhou 514015, China. [6]Australian Research Centre for Human Evolution, Griffith University, Brisbane 4111, Australia. [7]School of Social Science, University of Queensland, Brisbane, Australia. [8]Human Origins Program, National Museum of Natural History, Smithsonian Institution, Washington, DC 20560, USA. [9]The State Key Laboratory of Geohazard Prevention and Geoenvironment Protection (SKLGP), Chengdu University of Technology, Chengdu, Sichuan 610059, China. [10]Geography & Environmental Sciences, University of Southampton, Southampton SO17 1BJ, UK. [11]Lancaster Environment Centre, University of Lancaster, Bailrigg, Lancaster LA1 4YQ, UK.
*Corresponding author. Email: zhongping_lai@stu.edu.cn (Z.L.); htu@stu.edu.cn (H.T.)
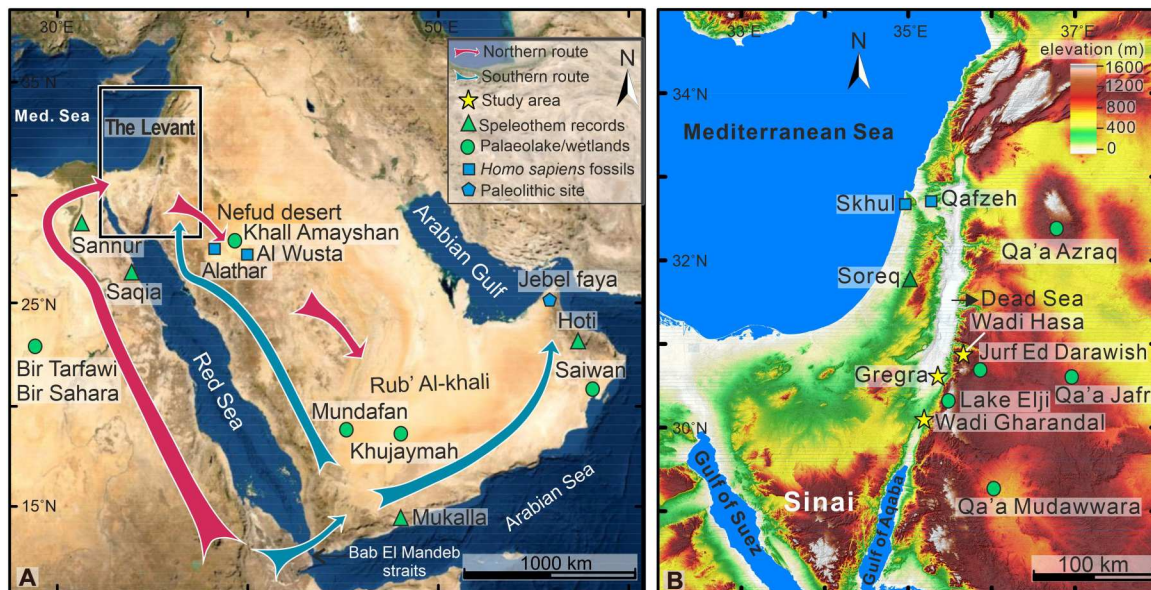
Fig. 1. Map showing archaeological, paleoclimatological, and paleoenvironmental records from the Levant and Arabia mentioned in the text. (**A**) The arrows indicate the suggested routes of human dispersals out of Africa [see (9, 17)]. The blue squares show sites with human fossils and footprints in northern Arabia, including those at Al Wusta paleolake (4) and Alathar paleolake (16), respectively. The green circles refer to paleolake/wetland sediments in the western desert of Egypt and Arabia, namely: Bir Tirfawi and Bir Sahara (52), Khall Amayshan (21), Mundafan (22), Khujaymah (22), and Saiwan (60). The green triangles show speleothem deposition in caves in the eastern desert of Egypt, including Saqia cave (43), Wadi Sannur (45), and in southern Arabia including Hoti cave in Oman and Mukkala cave in Yemen (23, 59). The main dated archaeological site in southeastern Arabia is Jebel Faya in the UAE (blue rhombus) (24, 58). (**B**) Digital elevation model map of the Levant showing the location of the study areas (yellow stars) along the Jordan Rift Valley (Wadi Gharandal and Gregra) and in the Jordanian Plateau (Wadi Hasa), and the paleolakes and speleothem records in the region. Paleolakes are represented by green circles, namely: Qa'a Azraq (53), Jurf Ed Darawish (26, 32), Lake Elji (54), Qa'a Jafr (27, 55), and Qa'a Mudawwara (28). Speleothem records in the Levant include Soreq cave (green triangle) (44, 46), and the blue squares show sites with human fossils including Skhul and Qafzeh caves (5). The source of digital elevation model data is derived from www.gscloud.cn.

Wadi Hasa

The Wadi Hasa sediment is composed of marl, rich in organic matter, with occasional black mats, voids, and sandy-silts and gravels (section HS1 in Fig. 2). The variation in stratigraphy indicates changes through time in the depositional environment. Marl can be white to tan in color but generally has a light green color; it contains root casts and burrows as well as plant remains and traces of plant roots, indicating deposition in a paludal environment with vegetation. The sharp change in lithology at site HS4 (fig. S1B), with sediments composed of poorly sorted pebbles, cobbles, and boulders, indicates the influence of flash floods in the wetland environment. The Wadi Hasa wetland was once dammed at an elevation of 779 m above sea level (a.s.l.) (refer to D1 in fig. S1B). The damming was previously determined (33) and confirmed in the present study as a consequence of rock debris accumulation from a landslide. Rockfalls were noted in the field at the south flank of the wadi along with debris flow deposits as likely mechanisms of prior damming, and the central part of the proposed dammed area consists of fluvial sediments composed mainly of angular, poorly sorted pebbles, cobbles, and boulders.

Luminescence dating results are listed in Table 1 and shown in the stratigraphic log (HS1 in Fig. 2). Quartz OSL ages from Wadi Hasa show that the deposition of the sediments occurred between 81 ± 5 ka and 43 ± 3 ka. At site HS1, the oldest age obtained from the basal part yielded an age of 81 ± 5 ka (HS2-OSL2, D_e of 146 Gy), and an age of 72 ± 5 ka (HS2-OSL1, D_e of 152 Gy) was obtained from the upper part of the same layer, indicating that the onset of wetland environment in the Wadi Hasa was during MIS 5a. The ages obtained from the middle and upper part of site HS1 are indicative of deposition during the period of ~53 to 42 ka. The summary of the earthquake history in the Dead Sea area showed a series of seismic events during the late Pleistocene (34), suggesting that the failure of the dam might be associated with earthquakes related to the activation of the Dead Sea Transform Fault.

Gregra

The wetland sediments of the Gregra area exhibit similar sedimentological characteristics as those noted in Wadi Hasa (fig. S1C), being mainly composed of light green marl, muddy sand and marly sand with root casts, rhizocretions, and Mn nodules. Angular gravels occur in the lower and middle parts of sections QR1 and QR2, indicating fluvial incision into the wetland facies (Fig. 2, QR1 and QR2). At site QR1, three feldspar multiple-elevated-temperature (MET) pIR-IRSL$_{250}$ ages were measured at the middle and upper part of the 6-m section as the lower part of the section is not exposed. The samples obtained from site QR1 yielded ages of 71 ± 4 ka (QR1-OSL2) and 45 ± 3 ka (QR1-OSL1). An age of 86 ± 7 ka (QR2-OSL1) at the basal part of site QR2 was equivalent to the basal part of site QR1. Thus, the onset of the incision was interpreted to occur before 86 ± 7 ka as marked by the deposition of poorly sorted fluvial gravel, while the formation of Gregra wetland was determined here to be within MIS 5c-a. The wetland sediments at site QR1 interfingered with fluvial sediments during the MIS 5/4 transition. The fluvial sediments at 71 ± 4 ka indicate

Table 1. Summary of luminescence dating results. Q, quartz; F, feldspar.

Sample ID*	Mineral	Depth (m)	K (%)	Th (ppm)	U (ppm)	Water content (%)	Total dose rate (Gy/ka)	Equivalent dose, D_e (Gy)	OD (%)	$2D_0$	Age (ka)
HS1-OSL1	Q	4.6	0.932 ± 0.093	5.48 ± 0.27	3.10 ± 0.15	20 ± 5	1.79 ± 0.09	96.7 ± 3.4	12 ± 3	154	54 ± 3
HS1-OSL2	Q	4.2	0.770 ± 0.077	4.53 ± 0.23	2.60 ± 0.13	20 ± 5	1.52 ± 0.07	86.6 ± 2.7	12 ± 2	155	57 ± 3
HS1-OSL3	Q	3.8	1.067 ± 0.106	6.27 ± 0.31	3.15 ± 0.16	20 ± 5	1.97 ± 0.10	92.3 ± 2.5	5 ± 2	151	47 ± 3
HS1-OSL4	Q	2.6	0.816 ± 0.081	5.14 ± 0.26	3.67 ± 0.18	20 ± 5	1.82 ± 0.09	79.3 ± 1.8	8 ± 2	136	43 ± 3
HS1-OSL5	Q	1.3	1.044 ± 0.104	5.93 ± 0.30	3.08 ± 0.15	20 ± 5	1.97 ± 0.10	91.5 ± 3.1	11 ± 2	147	46 ± 3
HS1-OSL6	Q	0.8	0.824 ± 0.082	4.62 ± 0.23	2.56 ± 0.13	20 ± 5	1.63 ± 0.08	69.6 ± 1.7	9 ± 2	137	43 ± 3
HS2-OSL1	Q	7.1	0.890 ± 0.089	5.80 ± 0.29	4.91 ± 0.24	20 ± 5	2.09 ± 0.10	152 ± 7	15 ± 3	155	72 ± 5
HS2-OSL2	Q	7.9	0.908 ± 0.090	5.29 ± 0.25	3.46 ± 0.17	20 ± 5	1.80 ± 0.08	146 ± 4	10 ± 2	168	81 ± 5
GH3-OSL2	Q	1.05	0.936 ± 0.093	3.69 ± 0.18	4.55 ± 0.23	20 ± 5	2.01 ± 0.09	144 ± 6	7 ± 3	155	71 ± 5
	F	1.05	0.936 ± 0.093	3.69 ± 0.18	4.55 ± 0.23	20 ± 5	2.68 ± 0.19	146 ± 15	30 ± 1	-	65 ± 10[†]
GH3-OSL3	Q	1.25	0.962 ± 0.096	3.92 ± 0.20	3.69 ± 0.18	20 ± 5	1.90 ± 0.093	161 ± 5	5 ± 3	154	84 ± 5
	F	1.25	0.962 ± 0.096	3.92 ± 0.20	3.69 ± 0.18	20 ± 5	2.57 ± 0.14	159 ± 3	28 ± 1	-	72 ± 6[†]
QR1-OSL1	F	0.3	0.930 ± 0.090	6.80 ± 0.34	2.78 ± 0.14	20 ± 5	2.61 ± 0.14	119 ± 1	2 ± 1	-	45 ± 3[‡]
QR1-OSL2	F	2.5	1.275 ± 0.127	9.17 ± 0.46	3.31 ± 0.16	20 ± 5	3.16 ± 0.17	223 ± 4	7 ± 2	-	71 ± 4[‡]
QR2-OSL1	F	5.3	1.516 ± 0.151	12.6 ± 0.63	9.66 ± 0.48	20 ± 5	5.25 ± 0.33	449 ± 23	16 ± 4	-	86 ± 7[‡]

*HS is for samples from Wadi Hasa; GH for Wadi Gharandal, and QR for Gregra.   † is for Feldspar pIR-IRSL$_{290}$ ages calculated using CAM model followed by fading rate correction, the g-values of which are 1.72 ± 0.48%/decade (GH3-OSL3) and 1.97 ± 0.81%/decade (GH3-OSL2), respectively.   ‡ is for feldspar ages using MET pIR-IRSL$_{250}$.

sporadic flood events, and then a shallow stagnant water environment occurred again until 45 ± 3 ka. The correlation of the feldspar ages of sites QR1 and QR2 indicated a humid period, before 45 ka, that allowed sedimentation of paludal sediments in the main valley.

DISCUSSION

Paleohydrological conditions in the Levant and Arabia played an important role during hominin dispersals (*4*, *16*, *17*). It is evident that a wide availability of water resources, due to increased precipitation in the Levant and Arabia, provided an opportunity for humans, herbivores, and carnivores to expand and survive over time (*4*, *16*) and that lake formation in Arabia supported human presence (*35*).

The luminescence ages show that Late Quaternary wetland sediments occurred in Wadi Gharandal (115 ± 8 to 71 ± 5 ka) (with Middle Paleolithic artifacts at 84 ± 5 ka) (Fig. 3B), Wadi Hasa (81 ± 5 to 43 ± 3 ka), and Gregra (86 ± 7 to 45 ± 3 ka). The presence of water could have allowed modern humans to migrate through a green corridor from Africa to Arabia and beyond. In contrast, most of the Paleolithic finds in Arabia were associated with paleolakes and wetland deposits within endorheic basins (*17*, *25*).

Dispersals out of Africa are believed to have taken place during times of substantially increased humidity and available freshwater resources (*25*, *36*). The Out of Africa dispersal scenario in MIS 5e has received major attention owing to the abundance of paleoenvironmental and archaeological archives during this ameliorated period (*7*, *12*, *13*, *19*, *37–39*). Human dispersals outside Africa have been perceived as both failures and successes (*40*), with MIS 5 dispersals considered as demographic failures and dispersals after 55 ka as successes (*38*, *41*). The dispersal route via the northern corridor from the Sinai Peninsula to the Levant and to Arabia (Fig. 1A) has been considered an optimum route as it was the only terrestrial route out of Africa (*17*, *42*). Dated fossils and archaeological evidence strongly supported the use of this corridor (Fig. 3 and references therein). Modern human fossils in the Levant were
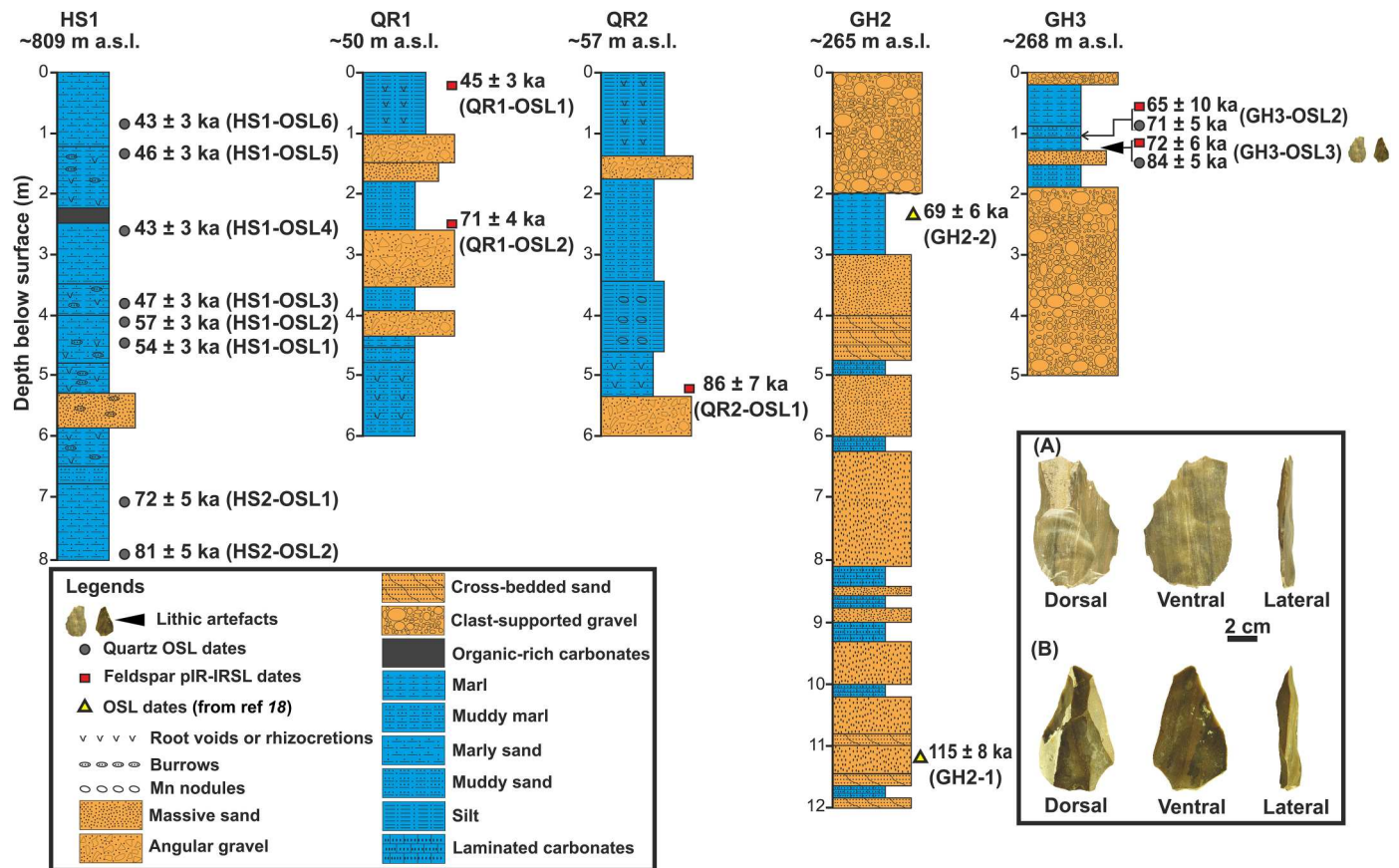
Fig. 2. Stratigraphic sections with luminescence ages of paludal sediments from Wadi Hasa (HS), Gregra area (QR), and Wadi Gharandal (GH). The inset shows lithic artifacts collected from site GH3. In (**A** and **B**) are the photographs of the two Levallois flakes. Both flakes include a faceted striking platform and a clear bulb of percussion. The light-colored zones are calcium carbonate accretions acquired after burial of the flakes [photograph from (*18*) with permission].

dated to be in 130 to 100 ka at Skhul and in 100 to 90 ka at Qafzeh caves (*5*). A human fossil and footprints, preserved in lake sediments at Al Wusta and Alathar paleolakes in northern Arabia, were dated to 95 to 85 ka and 115 ka, respectively, indicating that the southern Levant corridor was likely a route for human dispersals (Fig. 3A) (*4, 16*).

Paleoclimatic proxies from the northern route in MIS 5 showed wetter climate conditions with considerable precipitation in otherwise arid areas (Figs. 1 and 3, C to F) (*43, 44*). Speleothems from the eastern desert of Egypt showed growth during ~129 to 127 ka in Wadi Sannur and during ~130 to 83 ka in Saqia cave (*43, 45*). The southern Negev desert caves and the Soreq cave showed speleothem growth with enhanced precipitation during MIS 5e, MIS 5c, and MIS 5a, as well as at 55 ka (*44, 46–48*), congruent with the timing of sapropel formation in the Mediterranean Sea (*49, 50*).

Well-dated paleoclimatic records are essential for understanding the role of environmental change in promoting the movement of ancient human populations (Fig. 3B). The climatic and archaeological evidence in the Levant strongly supports the northern terrestrial route for the dispersal of large mammals (*51*). The chronology of Bir Tirfawi and Bir Sahara in the western desert of Egypt revealed the formation of paleolakes associated with Middle Stone Age tools during most of MIS 5 (*52*). In the Jordan desert, the chronology of paleolakes and paleowetlands was indicated at Qaʻa Azraq

(Qaʻa means depression) (*53*), Jurf Ed Darawish (*26, 32*), Lake Elji (*54*), Qaʻa Jafr (*27, 55*), and Qaʻa Mudawwara (*28*), indicating water resources availability facilitating human arrivals in Arabia either during MIS 5 and/or MIS 3. Our data show an agreement with the timing of the Dead Sea precursors: the last interglacial Lake Samra and the last glacial lake highstands (Fig. 3G) (*56, 57*). Further southward, the ages (falling in MIS 5, MIS 3, and the Holocene) of sediments of lakes and wetlands were in agreement with the ages of interbedded archaeological layers in Jebel Faya (*24, 58*), indicating multiple phases of human presence in the region (*21*). The timing of speleothem deposition in Hoti and Mukalla caves in southern Arabia (*23, 59*) was consistent with the formation of paleolakes, i.e., the Saiwan paleolake (*60*), the Khujaymah, and Mundafan lakes (*22*), during the MIS 5 and the Holocene (Figs. 1 and 3B). The links between climate, chronological, and archaeological data from the Levant and Arabia indicate that the Levant acted as a well-watered corridor in MIS 5 facilitating human dispersals.

MATERIALS AND METHODS
Sedimentary sections and sampling for the luminescence dating
The fieldwork surveys took place in 2017, 2018, and 2020 at Wadi Hasa, Gregra, and Wadi Gharandal. The sedimentology of four
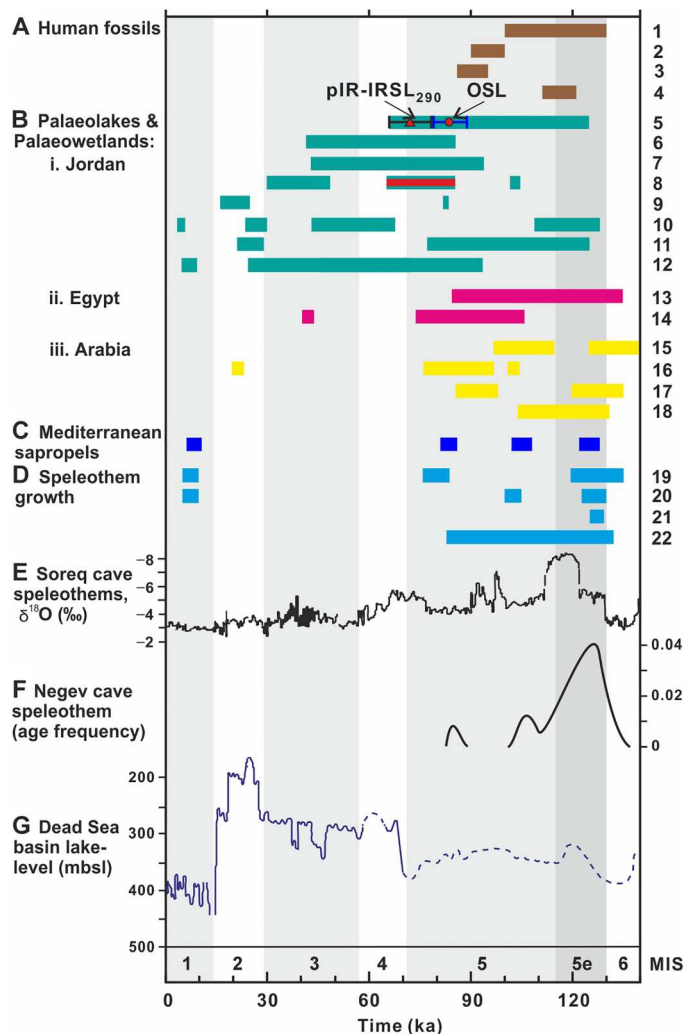
Fig. 3. Compilation of ages from this study with archaeological, paleoclimatic, and paleoenvironmental records from the Levant and Arabia since 140 ka. References for (**A**, **B**, **D**, and **E**) and site locations refer to Fig. 1 (A and B). References for the other sites are: (**C**) (*50*), (**F**) (*48*), (**G**) (*56*, *57*), and MIS records (*78*). The red line (Jurf Ed Darawish, site 9) and the quartz OSL and feldspar pIR-IRSL$_{290}$ ages of sample GH3-OSL3 at Wadi Gharandal (site 5) indicate the times of human presence. Archaeological and climatic records are: 1, Skhul cave; 2, Qafzeh cave; 3, Al Wusta; 4, Alathar; 5, Wadi Gharandal (study area); 6, Wadi Hasa (study area); 7, Gregra (study area); 8, Jurf Ed Darawish; 9, Qa'a Jafr; 10, Qa'a Azraq; 11, Qa'a Mudawwara; 12, Lake Elji; 13, Bir Tarfawi; 14, Bir Sahara; 15, Khall Amayshan; 16, Mundafan; 17, Khujaymah; 18, Saiwan; 19, Hoti cave; 20, Mukalla cave; 21, Wadi Sannur; and 22, Saqia cave.

exposed sections was investigated in the Wadi Hasa area at sites HS1, HS2, HS3, and HS4 (fig. S1B). Site HS1 has been sampled for OSL dating. The fieldwork focused on the entrance of the valley where lacustrine sediments are exposed at the margin near Hasa Umayyad castle (site HS1) to re-evaluate the chronology of these sediments that were previously dated by radiocarbon assay (unit C) (*31*). Site HS2 is located further downstream in the valley where Middle Paleolithic stone tools were found at the surface, and site HS4 is located downstream of the dam area (D1 in fig. S1B) determined by (*33*).

In the Wadi Hasa, sediments are deposited at relatively the same altitudes within the flat wide area at the entrance of the wadi, represented by site HS1, and the wadi narrows downstream. All sites are located on the northern side of the wadi, except site HS3, where the elevation is at its maximum: ca. 812 m a.s.l. in contrast to 809 m a.s.l. at site HS1. The elevation decreases gently westward of the valley reaching 800 m a.s.l. at site HS2 and 780 m a.s.l. at the location of the proposed former dam, and 759 m a.s.l. at site HS4 to below sea level near the Dead Sea. At site HS1, eight OSL samples were collected from an 8-m-thick exposure. A marked change in lithology is recorded downstream of the dam area, where boulders and poorly sorted cobbles at site HS4 indicate flash flood deposition. The elevations of the various sites were recorded using real-time kinematic (RTK) positioning within a global navigation satellite system (GNSS) with an uncertainty of 40 cm.

At Gregra, three wetland sedimentary sections were investigated, distributed over a wide area in a narrow valley and a flat upstream area (fig. S1C). The main purpose was to date the wetland sediments deposited along the margins of the valley at sites QR1 and QR2 located downstream. These sediments are deposited near the Proterozoic rocks of Jabal Hamra (Hamra Mountain) at an elevation of 50 and 63 m a.s.l., respectively.

The wetland sediments varied in thickness from 2 m upstream at the site QR3 to around 7 m at sites QR1 and QR2 downstream. The extension and depth of the paludal sediments were mapped. The elevations and extensions of the different units were recorded using a portable Garmin GPS. Two luminescence samples were collected from the middle and upper part of site QR1 to determine the minimum age of the sediments, while one OSL sample was collected from the basal part of site QR2 to determine the maximum age.

The fieldwork at Wadi Gharandal focused on obtaining luminescence samples for the in situ lithic tools reported in site GH3 (fig. S1A) (*18*). Two OSL samples were collected from site GH3, one from 20 cm above and another at the same elevation of the lithic tool.

At all sites, luminescence samples were collected by inserting 40-mm-diameter, 20-cm-long stainless-steel tubes into freshly exposed sediments. Subsequently, both ends of the tubes were sealed to prevent light exposure.

Luminescence analysis
Sample preparation and equipment
Thirteen sediment samples were opened under subdued red light in the luminescence dating laboratory of the Shantou University, Shantou, China. The sediment within 2 to 3 cm of the ends of the tubes was removed so that only unexposed sediments were used in the analyses. All samples were subject to standard procedures (*61*) using either quartz or feldspar. Among these samples, three, obtained from the Gregra area sites QR1 and QR2, were subject to feldspar MET pIR-IRSL. Two samples from Wadi Gharandal, GH3-OSL3 and GH3-OSL2, were measured using both quartz and feldspar (single grain) for age comparison due to potential quartz OSL signal saturation.

Samples were treated with HCl (10%) and H_2O_2 (30%) to remove carbonate and organic materials and then sieved to obtain 90- to 125- and 63- to 125-μm fractions according to fraction availability. For quartz OSL samples, both fractions were then etched by HF (40%) for 40 min to obtain pure quartz and to remove outermost layer exposed to α-particles and then washed for 20 min with HCl

(10%) to remove acid-soluble fluorides (*62*). A grain fraction of 63 to 125 μm was used for samples from section HS1 and 90 to 125 μm for samples from section GH3. Quartz grains were mounted in stainless steel discs using silicone oil in an area of ~5 mm in diameter. There could be several thousands of grains in an aliquot according to previous calculation (*63*). The purity of the quartz was checked by IRSL (*64*), and none of the samples contained a notable IRSL signal. For feldspar samples, the 90- to 125-μm fractions were used to concentrate feldspar by density separation (2.53 to 2.58 g/cm^3) using sodium polytungstate.

Luminescence measurements were performed on a Risø TL/OSL-DA-20 reader equipped with a $^{90}Sr/^{90}Y$ beta source. Quartz signals were stimulated by blue light-emitting diode (LED; 470 ± 20 nm) and recorded by a 9235QA photomultiplier through a 7.5-mm Hoya U-340 filter. Feldspar signals were stimulated by IR LED (870 ± 40 nm) for multiple grains aliquots and by IR laser (830 nm) for single-grain measurement and recorded by the same 9235QA photomultiplier through a combination of Schott BG39 and Corning 7-59 filters.

Preheat and dose recovery test

For quartz OSL samples, preheat plateau test have been applied on two representative samples, GH3-OSL2 and HS1-OSL1, from Wadi Gharandal and Wadi Hasa, respectively. Preheats following natural or regenerative doses at 200°, 220°, 240°, 260°, 280°, and 300°C with preheat following test doses 40°C lower were used for the modified single-aliquot regeneration (SAR) (*65*). Each preheat temperature was tested with three aliquots. Figure S2 (A and B) show results of preheat plateau between 220° to 300°C. The sizes of the given doses for the dose recovery experiments are 98 Gy for sample HS1-OSL1 and 138 Gy for sample GH3-OSL2. Acceptable dose recovery ratios for both samples are observed at the preheat of 260°C (fig. S2C). Therefore, a preheat at 260°C for 10 s and a subsequent preheat (following test dose) at 220°C for 10 s were selected for D_e measurements for all quartz OSL samples in this study. This approach is consistent with previous work on similar settings from Jordan wetland sediments (*18*).

For single-grain feldspar measurement, dose recovery tests were conducted applying two-step pIR-IRSL SAR protocol using three popular temperature combinations: pIR$_{50}$-IRSL$_{225}$, pIR$_{50}$-IRSL$_{290}$, and pIR$_{200}$-IRSL$_{225}$. First, 15 aliquots (~3 mm size) of feldspar from sample GH3-OSL3 were bleached in Hönle UVACUBE 400 solar simulator for 2 days. Then, these aliquots were separated into three groups (five aliquots each) and measured the residual dose (two aliquots) and dose recovery (three aliquots) applying the abovementioned three pIR-IRSL protocols. Residual dose is low (~5 Gy) and thus can be ignored for the investigated samples. For dose recovery test, a known dose close to the equivalent dose (202.4 Gy) was given, followed by a pIR-IRSL protocol, with a test dose (101.2 Gy) half of the given dose. The results showed that none of the given doses can be recovered for lower temperature (IRSL$_{50}$ or IRSL$_{200}$). However, for the higher temperatures of pIR$_{50}$-IRSL$_{290}$ or pIR$_{200}$-IRSL$_{290}$, the dose recovery ratios are within unity (0.90 ± 0.03 and 0.90 ± 0.04, respectively) (fig. S2D). Thus, we selected pIR$_{50}$-IRSL$_{290}$ as the protocol for D_e measurement and only used the IRSL$_{290}$ D_e for age calculation.

For the feldspar MET pIR-IRSL measurement, the IR stimulations at 50°, 100°, 150°, 200°, 250°, and 290°C with a preheat of 320°C were applied (*66, 67*). For dose recovery test (three aliquots), the modified SAR procedure was applied. A known dose close to the

equivalent dose (446.4 Gy) was given. The mean dose recovery ratio for the MET pIR-IRSL$_{250}$ signal was 1.05 ± 0.02, indicating that this protocol could recover a known dose. Figure S2E shows the dose recovery ratios of MET pIR-IRSL signals at 100°, 150°, 200°, 250°, 290°C were within 0.9 to 1.1. Given that (i) the highest anomalous fading is observed at 50°C, and it decreases to a negligible level as the stimulation temperature increases to ≥250°C (*67*), and (ii) dose recovery ratios at 250°C showed better concentration than 290°C, the MET pIR-IRSL$_{250}$ was used for D_e determination. The MET pIR-IRSL$_{250}$ signal also has been used for lacustrine sediments in the northeast Tibetan plateau [e.g., (*66*)].

D_e measurements

The quartz OSL signal was stimulated by blue LEDs at 130°C for 40 s. The initial 0.64 s of stimulation was integrated to construct a growth curve, after subtraction the background (last 1.6 s). D_e was measured by a combination of the SAR procedure (*65*) and the standard growth curve (SGC) procedure (*65, 68*). For each sample, six aliquots were first measured with a full SAR sequence to produce six D_es. These growth curves were then averaged to establish a sample-specific SGC (fig. S3, A and B), onto which the test dose (9.92 Gy) corrected natural OSL signals of c. 12 aliquots was projected to obtain D_es. The final D_e for a sample is the average of all D_es by both SAR and SGC. The shine-down curves of the OSL signals (fig. S3, A and B) showed that the signals decrease rapidly during the first second of stimulation, indicating that the OSL signal is dominated by fast component. The D_es of the OSL aliquots are normally distributed (fig. S4, A to D) with low overdispersion values (OD < 20%; also given in Table 1 for all samples). The 2D$_0$ values of all quartz OSL growth curves, calculated using exponential fitting, are less than the measured D_e (Table 1), except for GH3-OSL3, suggesting the validity of these quartz OSL ages.

All samples were first measured using quartz OSL. The initial test using quartz OSL for three samples from Gregra area (QR) showed that quartz OSL signals were saturated. Thus, we applied feldspar MET pIR-IRSL protocol for these samples. It has been reported that the MET pIR-IRSL (250°C) had negligible fading (*67, 69, 70*) and had low residual dose (21 Gy at most) for old samples (e.g., quartz signal saturated samples) (*67, 69, 70*).

In feldspar MET pIR-IRSL measurement, the test dose in dose recovery test was 81 Gy, ~18% of the given dose (446 Gy), and that in D_e measurement is 75 Gy, ~17% of estimated D_e (~450 Gy), both falling in the valid test dose range (*71, 72*). An example of shine-down curves of test dose of different SAR cycles showed that there is little dependence of the T_x signal to the preceding regeneration dose (fig. S3F). Typical shine-down curves of the MET pIR-IRSL$_{250}$ signals from sample QR2-OSL1 are shown in fig. S3E. The initial intensity of IRSL 50°C is the strongest, and the initial intensity of the MET pIR-IRSL signals has a general increasing trend toward higher temperatures. The dose-response curve of the MET pIR-IRSL$_{250}$ signal was fitted with an exponential plus linear function (fig. S3E). The MET pIR-IRSL$_{250}$ D_es are normally distributed (fig. S4, G and H) with low OD values (<20%, Table 1), suggesting that these samples in Jordan wetland settings are well bleached. The final D_e has been determined using the Central Age Model (CAM).

Feldspar single-grain technique was applied to the two most important samples (GH3-OSL2 and GH3-OSL3) for comparison of their quartz OSL ages, as sample GH3-OSL3 was collected from the same sediment layer containing the artifacts and GH3-OSL2 from just above the artifacts. For single-grain measurement,

pIR$_{50}$-IRSL$_{290}$, modified from (71), was used, but with IR laser instead of IR LED stimulation for the lower-temperature stimulation and without high-temperature wash at the end of each cycle. Preheat temperature of 320°C for 60 s was used before stimulation of IR laser at 50°C of 2 s and then 290°C of 2 s. We used the pIR-IRSL$_{290}$ signal for D_e calculation, because the IRSL signal at the higher temperature was considered to be suffering much less fading than that of the lower temperature and that the IRSL at lower temperature did not pass the dose recovery test (see preheat and dose recovery test section). A representative shine-down curve and dose-response curve for sample GH3-OSL3 are shown in fig. S3C. Test dose was 98.3 Gy, ~60 to 70% of the D_es, falling in the valid test dose range (71, 72). An example of shine-down curves of test dose of different SAR cycles (fig. S3D) showed that there is little dependence of the T_x signal to the preceding regeneration dose.

Results for each grain were accepted if they pass the rejection criteria: (i) recycling ratio within 10% of unity, (ii) maximum uncertainty in T_x less than 20%, (iii) maximum uncertainty in D_e less than 30%, (iv) maximum recuperation less than 5%, and (v) T_n signal more than three σ above BG. For 500 feldspar grains measured, 240 (GH3-OSL2) and 316 (GH3-OSL3) grains passed all criteria and gave D_e results. Symmetrical D_e distributions (fig. S4, E and F) indicated that these samples did not suffer from incomplete bleaching. Thus, CAM was applied for determining the final D_e. Fading test was performed on four multiple-grain aliquots lasting for up to ~15 days, and the final pIR-IRSL$_{290}$ age was corrected using attained g values (2.0 ± 0.8 and 1.7 ± 0.5 for the samples GH3-OSL2 and GH3-OSL3, respectively).

Dose rate measurement

The uranium and thorium content were measured using inductively coupled plasma mass spectrometry, whereas inductively coupled plasma optical emission spectrometry was used to determine the potassium content. The internal K and Rb concentrations in feldspar grains were assumed to be 12.5 ± 0.5% and 400 ± 100 parts per million (ppm), respectively (73). All these concentrations were converted to dose rate according to (74). The cosmic ray contribution was calculated on the basis of the altitude, geographical location, and depth of the samples (75). The water content was estimated as 20 ± 5% to accommodate that the uncertainty after deposition, in consideration of the extreme dryness (<1% water content) of the samples, as collected in the field, was not representative of their long-term water content. This consideration was especially relevant for samples associated with wetlands, which were likely to be intermittently saturated or, at times, submerged. For such samples, we assumed an average water content ranging between 15 and 25%. This decision was based on an assumption that the wetlands were saturated for a substantial fraction of the burial age. The estimated water content was consistent with similar settings in Jordan wetlands [e.g., (18, 32)]. The final dose rate and assigned ages in the present study were calculated using the LDAC program (76) for feldspar single-grain pIR-IRSL and the website program of DARC (77) for quartz OSL and feldspar MET pIR-IRSL.

Supplementary Materials

This PDF file includes:
Figs. S1 to S4
Provenance
References

REFERENCES AND NOTES

1. J.-J. Hublin, A. Ben-Ncer, S. E. Bailey, S. E. Freidline, S. Neubauer, M. M. Skinner, I. Bergmann, A. Le Cabec, S. Benazzi, K. Harvati, New fossils from Jebel Irhoud, Morocco and the pan-African origin of *Homo sapiens*. *Nature* **546**, 289–292 (2017).

2. I. McDougall, F. H. Brown, J. G. Fleagle, Stratigraphic placement and age of modern humans from Kibish, Ethiopia. *Nature* **433**, 733–736 (2005).

3. C. M. Vidal, C. S. Lane, A. Asrat, D. N. Barfod, D. F. Mark, E. L. Tomlinson, A. Z. Tadesse, G. Yirgu, A. Deino, W. Hutchison, A. Mounier, C. Oppenheimer, Age of the oldest known *Homo sapiens* from eastern Africa. *Nature* **601**, 579–583 (2022).

4. H. S. Groucutt, R. Grün, I. A. S. Zalmout, N. A. Drake, S. J. Armitage, I. Candy, R. Clark-Wilson, J. Louys, P. S. Breeze, M. Duval, L. T. Buck, T. L. Kivell, E. Pomeroy, N. B. Stephens, J. T. Stock, M. Stewart, G. J. Price, L. Kinsley, W. W. Sung, A. Alsharekh, A. al-Omari, M. Zahir, A. M. Memesh, A. J. Abdulshakoor, A. M. al-Masari, A. A. Bahameem, K. M. S. al Murayyi, B. Zahrani, E. L. M. Scerri, M. D. Petraglia, *Homo sapiens* in Arabia by 85,000 years ago. *Nat. Ecol. Evol.* **2**, 800–809 (2018).

5. R. Grün, C. Stringer, F. McDermott, R. Nathan, S. Porat, S. Robertson, L. Taylor, G. Mortimer, S. Eggins, M. McCulloch, U-series and ESR analyses of bones and teeth relating to the human burials from Skhul. *J. Hum. Evol.* **49**, 316–334 (2005).

6. I. Hershkovitz, G. W. Weber, R. Quam, M. Duval, R. Grün, L. Kinsley, A. Ayalon, M. Bar-Matthews, H. Valladas, N. Mercier, The earliest modern humans outside Africa. *Science* **359**, 456–459 (2018).

7. C. J. Bae, K. Douka, M. D. Petraglia, On the origin of modern humans: Asian perspectives. *Science* **358**, eaai9067 (2017).

8. J. Hill, A. Avdis, G. Bailey, K. Lambeck, Sea-level change, palaeotidal modelling and hominin dispersals: The case of the southern Red Sea. *Quat. Sci. Rev.* **293**, 107719 (2022).

9. M. D. Petraglia, P. S. Breeze, H. S. Groucutt, Blue Arabia, Green Arabia: Examining human colonisation and dispersal models, in *Geological setting, palaeoenvironment and archaeology of the Red Sea*, N. Rasul, I. Stewart, Eds. (Springer, 2019), pp. 675–683.

10. T. M. Rosenberg, F. Preusser, D. Fleitmann, A. Schwalb, K. Penkman, T. W. Schmid, M. A. Al-Shanti, K. Kadi, A. Matter, Humid periods in southern Arabia: Windows of opportunity for modern human dispersal. *Geology* **39**, 1115–1118 (2011).

11. E. Hölzchen, C. Hertler, C. Willmes, I. P. Anwar, A. Mateos, J. Rodríguez, J. O. Berndt, I. J. Timm, Estimating crossing success of human agents across sea straits out of Africa in the Late Pleistocene. *Palaeogeogr. Palaeoclimatol. Palaeoecol.* **590**, 110845 (2022).

12. M. D. Petraglia, M. Haslam, D. Q. Fuller, N. Boivin, C. Clarkson, Out of Africa: New hypotheses and evidence for the dispersal of *Homo sapiens* along the Indian Ocean rim. *Ann. Hum. Biol.* **37**, 288–311 (2010).

13. M. D. Petraglia, A. Parton, H. S. Groucutt, A. Alsharekh, Green Arabia: Human prehistory at the crossroads of continents. *Quat. Int.* **382**, 1–7 (2015).

14. I. Hershkovitz, H. May, R. Sarig, A. Pokhojaev, D. Grimaud-Hervé, E. Bruner, C. Fornai, R. Quam, J. L. Arsuaga, V. A. Krenn, A middle Pleistocene *Homo* from Nesher Ramla, Israel. *Science* **372**, 1424–1428 (2021).

15. O. Marder, O. Barzilai, T. Abulafia, I. Hershkovitz, M. Goder-Goldberger, Chrono-cultural considerations of middle paleolithic occurrences at Manot cave (western galilee), Israel, *The Middle and Upper Paleolithic Archeology of the Levant and Beyond*, (2018), pp. 49–63.

16. M. Stewart, R. Clark-Wilson, P. S. Breeze, K. Janulis, I. Candy, S. J. Armitage, D. B. Ryves, J. Louys, M. Duval, G. J. Price, P. Cuthbertson, M. A. Bernal, N. A. Drake, A. M. Alsharekh, B. Zahrani, A. al-Omari, P. Roberts, H. S. Groucutt, M. D. Petraglia, Human footprints provide snapshot of last interglacial ecology in the Arabian interior. *Sci. Adv.* **6**, eaba8940 (2020).

17. P. S. Breeze, H. S. Groucutt, N. A. Drake, T. S. White, R. P. Jennings, M. D. Petraglia, Palaeohydrological corridors for hominin dispersals in the Middle East ~250–70,000 years ago. *Quat. Sci. Rev.* **144**, 155–185 (2016).

18. B. S. Al-Saqarat, M. Abbas, Z. Lai, S. Gong, M. M. Alkuisi, A. M. B. A. Hamad, P. A. Carling, J. D. Jansen, A wetland oasis at Wadi Gharandal spanning 125–70 ka on the human migration trail in southern Jordan. *Quatern. Res.* **100**, 154–169 (2021).

19. R. M. Beyer, M. Krapp, A. Eriksson, A. Manica, Climatic windows for human migration out of Africa in the past 300,000 years. *Nat. Commun.* **12**, 4889 (2021).

20. J. E. Tierney, P. B. deMenocal, P. D. Zander, A climatic context for the out-of-Africa migration. *Geology* **45**, 1023–1026 (2017).

21. H. S. Groucutt, T. S. White, E. M. L. Scerri, E. Andrieux, R. Clark-Wilson, P. S. Breeze, S. J. Armitage, M. Stewart, N. Drake, J. Louys, G. J. Price, M. Duval, A. Parton, I. Candy, W. C. Carleton, C. Shipton, R. P. Jennings, M. Zahir, J. Blinkhorn, S. Blockley, A. al-Omari, A. M. Alsharekh, M. D. Petraglia, Multiple hominin dispersals into Southwest Asia over the past 400,000 years. *Nature* **597**, 376–380 (2021).

22. A. Matter, E. Neubert, F. Preusser, T. Rosenberg, K. Al-Wagdani, Palaeo-environmental implications derived from lake and sabkha deposits of the southern Rub' al-Khali, Saudi Arabia and Oman. *Quat. Int.* **382**, 120–131 (2015).

23. D. Fleitmann, S. J. Burns, M. Pekala, A. Mangini, A. Al-Subbary, M. Al-Aowah, J. Kramers, A. J. Q. S. R. Matter, Holocene and Pleistocene pluvial periods in Yemen, southern. *Quat. Sci. Rev.* **30**, 783–787 (2011).

24. S. J. Armitage, S. A. Jasim, A. E. Marks, A. G. Parker, V. I. Usik, H.-P. Upermann, The southern route "out of Africa": Evidence for an early expansion of modern humans into Arabia. *Science* **331**, 453–456 (2011).

25. S. L. Nicholson, R. Hosfield, H. S. Groucutt, A. W. G. Pike, D. Fleitmann, Beyond arrows on a map: The dynamics of *Homo sapiens* dispersal and occupation of Arabia during Marine Isotope Stage 5. *J. Anthropol. Archaeol.* **62**, 101269 (2021).

26. K. Moumani, J. Alexander, M. D. Bateman, Sedimentology of the late Quaternary Wadi Hasa Marl Formation of central Jordan: A record of climate variability. *Palaeogeogr. Palaeoclimatol. Palaeoecol.* **191**, 221–242 (2003).

27. C. P. Davies, Quaternary paleoenvironments and potential for human exploitation of the Jordan Plateau desert interior. *Geoarchaeology* **20**, 379–400 (2005).

28. N. Petit-Maire, P. Carbonel, J.-L. Reyss, P. Sanlaville, A. Abed, R. Bourrouilh, M. Fontugne, S. Yasin, A vast Eemian palaeolake in Southern Jordan (29 N). *Global Planet. Change* **72**, 368–373 (2010).

29. M. Abbas, B. Al-Saqarat, A. Al-Shdaifat, Paleoclimate reconstruction of the quaternary sediments near the Gulf of Aqaba (Southern Jordan). *Arab. J. Geosci.* **9**, 1–13 (2016).

30. G. A. Catlett, J. A. Rech, J. S. Pigati, M. Al Kuisi, S Li, J. S. Honke, Activation of a small ephemeral lake in southern Jordan during the last full glacial period and its paleoclimatic implications. *Quatern. Res.* **88**, 98–109 (2017).

31. J. A. Rech, H. Ginat, G. Catlett, S. Mischke, E. Winer-Tully, J. S. Pigati, Pliocene-Pleistocene water bodies and associated geologic deposits in Southern Israel and Southern Jordan, in *Quaternary of the Levant: Environments, Climate Change, and Humans*, Y. Enzel, O. Bar-Yosef, Eds., (Cambridge University Press, 2017), pp. 127–134.

32. S. Mischke, Z. Lai, G. Faershtein, N. Porat, M. Röhl, P. Braun, J. Kalbe, H. Ginat, A late pleistocene wetland setting in the Arid Jurf ed Darawish Region in Central Jordan. *Front. Earth Sci.* **9**, 722435 (2021).

33. J. Schuldenrein, G. A. Clark, Landscape and prehistoric chronology of West-Central Jordan. *Geoarchaeology* **9**, 31–55 (1994).

34. Y. Lu, J. Moernaut, N. Waldmann, R. Bookman, G. Ian Alsop, A. Hubert-Ferrari, M. Strasser, A. Agnon, S. Marco, Orbital- and millennial-scale changes in lake-levels facilitate earthquake-triggered mass failures in the dead sea Basin. *Geophys. Res. Lett.* **48**, e2021GL093391 (2021).

35. M. Engel, A. Matter, A. G. Parker, A. Parton, M. D. Petraglia, G. W. Preston, F. Preusser, Lakes or wetlands? A comment on 'The middle Holocene climatic records from Arabia: Reassessing lacustrine environments, shift of ITCZ in Arabian Sea, and impacts of the southwest Indian and African monsoons' by Enzel et al. *Global Planet. Change* **148**, 258–267 (2017).

36. H. F. Lamb, C. R. Bates, C. L. Bryant, S. J. Davies, D. G. Huws, M. H. Marshall, H. M. Roberts, H. Toland, 150,000-year palaeoclimate record from northern Ethiopia supports early, multiple dispersals of modern humans from Africa. *Sci. Rep.* **8**, 1077 (2018).

37. A. Frumkin, O. Bar-Yosef, H. P. Schwarcz, Possible paleohydrologic and paleoclimatic effects on hominin migration and occupation of the Levantine Middle Paleolithic. *J. Hum. Evol.* **60**, 437–451 (2011).

38. E. A. A. Garcea, Successes and failures of human dispersals from North Africa. *Quat. Int.* **270**, 119–128 (2012).

39. H. S. Groucutt, M. D. Petraglia, G. Bailey, E. M. L. Scerri, A. Parton, L. Clark-Balzan, R. P. Jennings, L. Lewis, J. Blinkhorn, N. A. Drake, P. S. Breeze, R. H. Inglis, M. H. Devès, M. Meredith-Williams, N. Boivin, M. G. Thomas, A. Scally, Rethinking the dispersal of *Homo sapiens* out of Africa. *Evol. Anthropol.* **24**, 149–164 (2015).

40. R. J. Rabett, The success of failed *Homo sapiens* dispersals out of Africa and into Asia. *Nat. Ecol. Evol.* **2**, 212–219 (2018).

41. J. J. Shea, Transitions or turnovers? Climatically-forced extinctions of *Homo sapiens* and Neanderthals in the east Mediterranean Levant. *Quat. Sci. Rev.* **27**, 2253–2270 (2008).

42. O. Bar-Yosef, A. Belfer-Cohen, Following Pleistocene road signs of human dispersals across Eurasia. *Quat. Int.* **285**, 30–43 (2013).

43. F. Henselowsky, R. Eichstädter, A. Schröder-Ritzrau, D. Herwartz, A. Almoazamy, N. Frank, K. Kindermann, O. Bubenzer, Speleothem growth phases in the central Eastern Desert of Egypt reveal enhanced humidity throughout MIS 5. *Quat. Int.* **657**, 26–36 (2021).

44. M. Bar-Matthews, J. Keinan, A. Ayalon, Hydro-climate research of the late Quaternary of the Eastern Mediterranean-Levant region based on speleothems research–A review. *Quat. Sci. Rev.* **221**, 105872 (2019).

45. M. I. El-Shenawy, S.-T. Kim, H. P. Schwarcz, Y. Asmerom, V. J. Polyak, Speleothem evidence for the greening of the Sahara and its implications for the early human dispersal out of sub-Saharan Africa. *Quat. Sci. Rev.* **188**, 67–76 (2018).

46. M. Bar-Matthews, A. Ayalon, M. Gilmour, A. Matthews, C. J. Hawkesworth, Sea–Land oxygen isotopic relationships from planktonic foraminifera and speleothems in the Eastern Mediterranean region and their implication for paleorainfall during interglacial intervals. *Geochim. Cosmochim. Acta* **67**, 3181–3199 (2003).

47. A. Vaks, M. Bar-Matthews, A. Ayalon, A. Matthews, L. Halicz, A. Frumkin, Desert speleothems reveal climatic window for African exodus of early modern humans. *Geology* **35**, 831–834 (2007).

48. A. Vaks, M. Bar-Matthews, A. Matthews, A. Ayalon, A. Frumkin, Middle-Late Quaternary paleoclimate of northern margins of the Saharan-Arabian Desert: Reconstruction from speleothems of Negev Desert, Israel. *Quat. Sci. Rev.* **29**, 2647–2662 (2010).

49. K. M. Grant, R. Grimm, U. Mikolajewicz, G. Marino, M. Ziegler, E. J. Rohling, The timing of Mediterranean sapropel deposition relative to insolation, sea-level and African monsoon changes. *Quat. Sci. Rev.* **140**, 125–141 (2016).

50. M. Rossignol-Strick, Mediterranean Quaternary sapropels, an immediate response of the African monsoon to variation of insolation. *Palaeogeogr. Palaeoclimatol. Palaeoecol.* **49**, 237–263 (1985).

51. M. Stewart, J. Louys, G. J. Price, N. A. Drake, H. S. Groucutt, M. D. Petraglia, Middle and Late Pleistocene mammal fossils of Arabia and surrounding regions: Implications for biogeography and hominin dispersals. *Quat. Int.* **515**, 12–29 (2019).

52. K. Nicoll, A revised chronology for Pleistocene paleolakes and Middle Stone Age–Middle Paleolithic cultural activity at Bîr Tirfawi–Bîr Sahara in the Egyptian Sahara. *Quat. Int.* **463**, 18–28 (2018).

53. C. J. H. Ames, C. E. Cordova, K. Boyd, C. Schmidt, D. Degering, J. Kalbe, B. G. Jones, A. Dosseto, J. T. Pokines, A. S. Alsouliman, Middle to Late Quaternary palaeolandscapes of the central Azraq Basin, Jordan: Deciphering discontinuous records of human-environment dynamics at the arid margin of the Levant. *Quat. Int.* **635**, 31–52 (2022).

54. N. Abu-Jaber, S. Al Khasawneh, M. Alqudah, C. Hamarneh, A. Al-Rawabdeh, A. Murray, Lake Elji and a geological perspective on the evolution of Petra, Jordan. *Palaeogeogr. Palaeoclimatol. Palaeoecol.* **557**, 109904 (2020).

55. P. G. Macumber, Evolving landscape and environment in Jordan, *The archaeology of Jordan* (2001), pp. 1-30.

56. Y. Bartov, S. L. Goldstein, M. Stein, Y. Enzel, Catastrophic arid episodes in the Eastern Mediterranean linked with the North Atlantic Heinrich events. *Geology* **31**, 439–442 (2003).

57. N. Waldmann, M. Stein, D. Ariztegui, A. Starinsky, Stratigraphy, depositional environments and level reconstruction of the last interglacial Lake Samra in the Dead Sea basin. *Quatern. Res.* **72**, 1–15 (2009).

58. K. Bretzke, F. Preusser, S. Jasim, C. Miller, G. Preston, K. Raith, S. J. Underdown, A. Parton, A. G. Parker, Multiple phases of human occupation in Southeast Arabia between 210,000 and 120,000 years ago. *Sci. Rep.* **12**, 1600 (2022).

59. D. Fleitmann, S. J. Burns, M. Mudelsee, U. Neff, J. Kramers, A. Mangini, A. Matter, Holocene forcing of the Indian monsoon recorded in a stalagmite from southern Oman. *Science* **300**, 1737–1739 (2003).

60. T. M. Rosenberg, F. Preusser, I. Blechschmidt, D. Fleitmann, R. Jagher, A. Matter, Late Pleistocene palaeolake in the interior of Oman: A potential key area for the dispersal of anatomically modern humans out-of-Africa? *J. Quat. Sci.* **27**, 13–16 (2012).

61. M. J. Aitken, *Introduction to optical dating: The dating of Quaternary sediments by the use of photon-stimulated luminescence* (Clarendon Press, 1998).

62. Z.-P. Lai, A. G. Wintle, Locating the boundary between the Pleistocene and the Holocene in Chinese loess using luminescence. *Holocene* **16**, 893–899 (2006).

63. G. A. T. Duller, Single-grain optical dating of Quaternary sediments: Why aliquot size matters in luminescence dating. *Boreas* **37**, 589–612 (2008).

64. Z. Lai, H. Brückner, Effects of feldspar contamination on equivalent dose and the shape of growth curve for OSL of silt-sized quartz extracted from Chinese loess. *Geochronometria* **30**, 49–53 (2008).

65. H. M. Roberts, G. A. T. Duller, Standardised growth curves for optical dating of sediment using multiple-grain aliquots. *Radiat. Meas.* **38**, 241–252 (2004).

66. Z. Ding, L. Yu, Z. Lai, P. An, X. Miao, R. Xu, Z. Liu, Post-IR IRSL chronology of paleo-lacustrine sediments from yardangs in the Qaidam Basin, NE Tibetan Plateau. *Geochronometria* **48**, 313–324 (2021).

67. B. Li, S.-H. Li, Luminescence dating of K-feldspar from sediments: A protocol without anomalous fading correction. *Quat. Geochronol.* **6**, 468–479 (2011).

68. Z. Lai, Testing the use of an OSL standardised growth curve (SGC) for determination on quartz from the Chinese Loess Plateau. *Radiat. Meas.* **41**, 9–16 (2006).

69. B. Li, S. Li, A reply to the comments by Thomsen et al. on "Luminescence dating of K-feldspar from sediments: A protocol without anomalous fading correction". *Quat. Geochronol.* **8**, 49–51 (2012).

70. X. Fu, T. J. Cohen, L. J. Arnold, Extending the record of lacustrine phases beyond the last interglacial for Lake Eyre in central Australia using luminescence dating. *Quat. Sci. Rev.* **162**, 88–110 (2017).

71. C. Thiel, J.-P. Buylaert, A. Murray, B. Terhorst, I. Hofer, S. Tsukamoto, M. Frechen, Luminescence dating of the Stratzing loess profile (Austria)–Testing the potential of an elevated temperature post-IR IRSL protocol. *Quat. Int.* **234**, 23–31 (2011).

72. D. Colarossi, G. A. T. Duller, H. M. Roberts, Exploring the behaviour of luminescence signals from feldspars: Implications for the single aliquot regenerative dose protocol. *Radiat. Meas.* **109**, 35–44 (2018).

73. D. J. Huntley, M. R. Baril, The K content of the K-feldspars being measured in optical dating or in thermoluminescence dating. *Ancient TL* **15**, 11–13 (1997).

74. G. Guérin, N. Mercier, R. Nathan, G. Adamiec, Y. Lefrais, On the use of the infinite matrix assumption and associated concepts: A critical review. *Radiat. Meas.* **47**, 778–785 (2012).

75. J. R. Prescott, J. T. Hutton, Cosmic ray contributions to dose rates for luminescence and ESR dating: Large depths and long-term time variations. *Radiat. Meas.* **23**, 497–500 (1994).

76. P. Liang, S. L. Forman, LDAC: An Excel-based program for luminescence equivalent dose and burial age calculations. *Ancient TL* **37**, 21–40 (2019).

77. J. A. Durcan, G. E. King, G. A. T. Duller, DRAC: Dose rate and age calculator for trapped charge dating. *Quat. Geochronol.* **28**, 54–61 (2015).

78. L. E. Lisiecki, M. E. Raymo, A Pliocene-Pleistocene stack of 57 globally distributed benthic $\delta^{18}O$ records. *Paleoceanography* **20**, 1–17 (2005).